Micromechanics of sea ice frictional slip from test basin scale experiments

Peter R. Sammonds[1], Daniel C. Hatton[1,2] and Daniel L. Feltham[3]

*[1]Rock and Ice Physics Laboratory, Department of Earth Sciences, University College London, Gower Street, London, UK WC1E 6BT (*p.sammonds@ucl.ac.uk). [2]School of Marine Science and Engineering, Plymouth University, Drake Circus, Plymouth, UK PL4 8AA. [3]Centre for Polar Observation and Modelling, Department of Meteorology, University of Reading, PO Box 243, Reading, UK RG6 6BB*

*Author for correspondence (p.sammonds@ucl.ac.uk)

Keywords: sea ice friction; micromechanics; scaling

Summary

We have conducted a series of high-resolution friction experiments on large floating saline ice floes in an environmental test basin. In these experiments, a central ice floe was pushed between two other floes, sliding along two interfacial faults. The frictional motion was predominantly stick-slip. Shear stresses, normal stresses, local strains and slip displacement were measured along the sliding faults, and acoustic emissions were monitored. High resolution measurements during a single stick-slip cycle at several positions along the fault allowed us to identify two phases of frictional slip: a nucleation phase, where a nucleation zone begins to slip before the rest of the fault, and a propagation phase when the entire fault is slipping. This is slip-weakening behaviour. We have therefore characterized what we consider to be a key deformation mechanism in Arctic Ocean dynamics.

In order to understand the micromechanics of sea ice friction, we have employed a theoretical constitutive relation (i.e., an equation for shear stress in terms of temperature, normal load, acceleration, velocity and slip displacement) derived from the physics of asperity-asperity contact and sliding [1]. We find our experimental data conform reasonably with this frictional law once slip weakening is introduced. We find the constitutive relation follows Archard's law rather than Amontons's law, with $\tau \propto \sigma_n{}^n$ (where τ is the shear stress and σ_n is the normal stress) and $n = 26/27$, with a fractal asperity distribution, where the frictional shear stress, $\tau = f_{fractal}\, T_{ml}\, w_s$, where $f_{fractal}$ is the fractal asperity height distribution, T_{ml} is the shear strength for frictional melting and lubrication and w_s is the slip weakening. We can therefore deduce the interfacial faults failed in shear for these experimental conditions through processes of brittle failure of asperities in shear, and at higher velocities, frictional heating, localized surface melting and hydrodynamic lubrication.

1. Introduction

Understanding ice friction is important across many scales. At the micro-scale, fundamental physical processes of asperity contact affect icing on structures and friction in winter sports [2]; at intermediate scales in arctic engineering ice friction determines the resistance to ship movement [3], or in glaciology, ice stream dynamics [4]; at the Arctic Basin scale, ice friction is a control on the distribution and thickness of sea ice [5]; on a planetary scale, friction has a role in planetary dynamics [6]. However, ice friction is also a controversial topic involving complex processes such as fracture, creep, pressure melting, pre-melting and frictional heating [1]. In this paper we address

the micromechanics of sea ice friction, derived from intermediate scale experiments, in order that they might be upscaled to the Arctic Basin scale.

Sea ice is notably brittle [7]. In the Arctic Ocean, ice deformation causes formation of thin ice through creation and subsequent refreezing of open-water leads and thick ice through ice rafting and ridging. RADARSAT imagery shows that the most salient features of the arctic sea ice cover during winter are the presence of long lineaments, some of which extend across large parts of the Arctic Basin and show high shear deformation [8]. Marko and Thomson (1997) [9] suggested that these lineaments are analogous to strike-slip faults in the Earth's crust. Friction plays a key role in ice rafting and ridging [10]. Stick-slip friction has been observed in laboratory experiments on multi-year sea ice [7] and one can deduce that it plays a key role in sea ice dynamics and explains behaviour observed in ice tank experiments [11]. So it is clear that a realistic sea ice rheology has to incorporate discontinuous slip displacement on these faults [12]. For upscaling, Taylor et al. (2006) [13] have proposed a homogenization methodology to determine a continuum-scale sea ice rheology from consideration of ice interactions within a representative region to enable the upscaling.

Laboratory experimental work on the mechanics of ice friction has shown that at high enough sliding speeds, the low friction of ice is caused by a lubricating layer of melt water generated by frictional heating [14]. The water-lubrication mechanism has been investigated by Evans et al. (1976) [15] in the laboratory using a slider block and modelled by Oksanen and Keinonen (1982) [16] and Nielsen et al. (2008) [17]. Persson (2015) [18] proposed that softening results in a thin layer of disordered ice, with a shear strength which decreases continuously as the ice surface temperature approaches the bulk melting temperature at intermediate speeds. At low sliding speeds, over the velocity domain from 0.01 $mm.s^{-1}$ to 100 $mm.s^{-1}$, where frictional heating does not play a role, the coefficient of friction of ice can be considerably higher. Rist (1997) [19] attributes this to elastically deforming asperities undergoing shear fracture. Plastic creep deformation and adhesion have also been proposed as the cause of higher friction [20, 21, 22, 23]. Hatton et al. (2009) [1] constructed a theoretical procedure for predicting which mechanisms of normal deformation (ductile or elastic) and shear failure (ductile, brittle, or melting and hydrodynamic lubrication) will apply under particular circumstances, so unifying the various micro-mechanical perspectives.

Ice friction is usually modelled by Amontons's classical friction law, $\tau = \mu\sigma$, where τ is the shear stress, μ is the coefficient of friction, and σ is the normal stress [e.g., 14] or by Coulomb's law which introduces a cohesive term [e.g., 23]. (See Table 1 for a list of symbols.) Rist's (1997) [19] re-analysis of ice friction data where surface melting is unlikely to occur, favours a non-linear friction law in which $\tau \propto \sigma^{2/3}$, in accordance with Archard's (1957) law [24]. Lishman et al. (2011) [25] introduced a rate and state friction law which combined the classical frictional law with phenomenological curves for the dependence of shear stress on sliding velocity and on the time for which the ice has been stationary. But in rock and earthquake mechanics [26], it has been recognised that the frictional slip displacement is an important parameter. This has received little attention in ice mechanics and we would argue that this, or slip time [27] needs to be included explicitly in rheological models of arctic sea ice.

In order to characterize ice floe friction, we have conducted intermediate scale experiments in an environmental test basin, usually employed for testing model ships, where large floating saline ice floes were pushed past each other in double direct shear (described in Section 2). Intermediate scale experiments lend confidence that the results can be up-scaled while at the same time precise measurements can be made of shear stress on the fault, slip displacement, ambient temperature, normal stress on the interfacial faults, sliding velocity and the hold time for which the ice has been

static [25]. This gives a level of resolution usually associated with small scale laboratory tests [e.g., 26] but not achievable in experiments in the Arctic Ocean due to the hostile environment [e.g., 2]. In Section 3, we present our results in terms of the spatial-temporal representation of slip in the rock and earthquake mechanics nucleation and propagation process. In Section 4 we discuss the results and unifying approaches across scales. In Section 5 we model our experimental results using the micromechanical friction law of Hatton et al. (2009) [1]. In Section 6 we discuss the implications of our results and conclude with a suitable form for the friction law that could be applied at an Arctic Basin scale.

2 Experimental method

2.1 Test basin experiments

For our experiments, we used the Arctic Environmental Test Basin of the Hamburgische Schiffbau-Versuchsanstalt (HSVA), Hamburg (Fig. 1) [28]. The concrete basin is 30m long, 6m wide and 1.2m deep and filled with saline water, with salinity approximately 35 ppt; the same as ocean water. A motorized bridge spans the basin, on which is mounted a carriage for the operator. Air temperature can be regulated between -20°C to +20°C to cool the basin. To produce an ice sheet, saline water from the basin is sprayed onto the water surface to produce an ice skim and then the overlying air temperature is lowered to grow the ice sheet. An ice sheet may be grown at an initial rate of up to 2 mm thickness per hour, but as the sheet thickens the growth rate slows considerably. Once the ice sheet has been grown to roughly the desired thickness the air temperature is then set to the desired test temperature. The effect of this is to produce a saline ice sheet, with roughly controllable thickness, of predominantly columnar- grained ice.

An ice sheet was grown at a nominal air temperature of -15°C to an average thickness of 168mm over several days. Over the 3-day course of our experiments the ice sheet continued to thicken slowly. The thickness was monitored by auguring in several places on the ice sheet, twice a day. The difference in ice sheet thickness across its expanse was 8mm. For day 1 and day 2 the average air temperature in the test basin was -7°C; the ice sheet thickened by 2mm on average. For day 3 the average air temperature was -11°C and the ice sheet thickened to 174mm on average. The time for the ice sheet to respond to a new set temperature was about 15h. Air temperature was monitored continuously at four locations in the ice basin chamber, 2m above the ice sheet, and water temperature at three locations along the length of the basin at different depths. The air temperature showed a gradient of about 2°C along the length of the ice sheet and about 0.5°C across its width, and was controlled to better than 1°C during a day. The water temperature showed remarkable consistency being -2.3°C at the shallower depth and -2.1°C at deeper depths with no measurable variations. The temperature profile of the ice sheet was monitored continuously by a thermistor string embedded in the ice sheet.

Temperature profiles of the ice sheet recorded during two friction tests on day 1 and day 2 are shown in figure 2. Temperature was stable during each test. These roughly S-shape to linear profiles are both indicative of basal freezing and bottom accumulation conditions. Thin sections taken from a block cut from the ice sheet at the end of the experimental program are shown in figure 3, viewed under cross polarizing lenses. Two parallel sets of thick sections were cut perpendicular to the length of the test basin and one set of thick sections were cut parallel to its length. Three horizontal thick sections were cut at depths of 15 mm, 90 mm and 180mm in the plane of the ice sheet. Thin sections were made using standard techniques. A pair of representative vertical sections, cut through the thickness of the ice sheet, and two horizontal sections at 15 mm and 90 mm depth are shown. The sections show that the ice sheet consists of a layer of fine grained granular ice at the top, but

columnar grain growth is quickly established, with a columnar grain width of over 10mm on average (Fig 3a). Surface roughness of the sliding fault surfaces were measured. In figure 3b a surface topographic profile is shown. Casts were made of surfaces using a quick-curing, high-resolution rubber solution (Microset 101RF) and the surface profile measured using a Proscan optical profilometer. These data are presented in Hatton et al. (2009) [1] Supplementary Material. As discussed, we believe that this surface topography is controlled primarily by the sliding process producing a fractal surface [30]. We suggest that sea ice floes in the Arctic Ocean, which have undergone a similar repeated-sliding process, will have similar topography.

2.2 Friction experiments

The configuration for our experiments was the double-direct shear friction test (or mode II fracture mechanics test), analogous to that used in small-scale rock mechanics experiments [e.g., 26]. As shown in figure 4, a central free-floating ice floe (B), measuring 1.2 m by 6.5 m was pushed between two floating ice floes (A and C) along parallel pre-cut faults. The central floe was pushed by pusher plate mounted on the motorized rail-mounted bridge which spans the width of the test basin (Fig. 1). The bridge can move at nominal speeds ranging from 210 μm.s^{-1} to 7 mm.s^{-1}. The load normal to the fault surfaces was applied by six air-activated actuators mounted as pairs on three floating wooden frames (Fig. 4). Normal load was set by the air pressure driving the actuators. The ice floes were prepared for experiments by cutting the ice sheet using a pair of cutters mounted on the test basin bridge. In this way parallel faults were ensured.

The instrumentation set-up is shown schematically in figure 4 and can be seen in figure 1. Frictional load (F) was measured by two 20kN load cells mounted between the pusher plate and the cantilever attaching it to the carriage of test basin bridge. Normal load (N) was measured by six 10kN load cells mounted in pairs on the pneumatic rams on the floating normal load frames. The slip displacements (D_j, $j \in \{1,2,3,...,8\}$) on the central floe relative to the outer floe were measured by four 1m long stroke potentiometer displacement transducers mounted along each of the interfacial faults. Normal displacements were measured by a series of six 20mm stroke potentiometer displacement transducers, spaced at 1 m intervals, mounted across the fault. Local shear stresses (τ_i, $i \in \{1, 2, 3, \ldots, 8\}$) were measured by 16 stress sensors frozen into the ice floe and mounted in pairs as two limbs of rosettes. These stress sensors were 100 mm diameter mercury pressure pads [29]. Eight acoustic transducers were frozen onto the ice to monitor and locate acoustic emissions.

We undertook a series of lubricated double-direct shear friction tests on saline ice floes over a range of nominal speeds from 210μm.s^{-1} to 7mm.s^{-1}, a series of hold times, two set air temperatures, -7°C and -11°C, and a range of normal loads from 0 to 100kN. There were 22 experimental runs (Table 2). When the frictional load (F) was applied by the test basin bridge to the central ice floe either frictional sliding took place or the floe would not move. Frictional sliding took a stick-slip form, where shear load was applied the central ice floe remains stationary for some time, while clearly-visible flexural strain built up in the pusher plate, before the central ice floe suddenly and briefly moved forward, allowing the flexural strain in the pusher plate to relax; this cycle was then repeated, as long as the bridge kept driving forward. An example of results from an experiment is shown in figure 5. Here shear stress in the central ice floe is plotted against the slip displacement of the floe for several stick-slip cycles, chosen arbitrarily from a complete run. (The origin is arbitrary.) In this experiment the frictional force was applied at a nominal speed of 2.1mm.s^{-1}. The nominal air temperature was -7°C; the ice floe temperature profile measured during this test is shown in figure 2 (the colder of the two temperature profiles). The typical normal load was 75kN, however no positive side load was applied by the actuators in this test.

2.3 Note on calibration

All force and stress measuring instruments were calibrated, prior to installation in the test basin by compressing them in series with the same load cell, of known sensitivity, offset and cross-sectional area. Similarly, all displacement-measuring instruments were calibrated against a steel rule. Visual inspection of plots of the output voltage against displacement, load or pressure of the instruments, as appropriate, confirmed their linearity, and least squares fitting was used to determine their sensitivities and offsets.

The freezing of the mercury stress sensors into the ice sheet and the bolting of the load cells to the pusher plate and to the normal load frames, were all capable of applying some force to the instruments and introducing extra offsets; in the first of these cases, the timescale-dependent and temperature- dependent mechanical properties of ice meant that the offset could vary with time. For the pusher plate load cells, this offset was determined, by taking the arithmetic mean of measurements of force F, during an experiment (no. 2-1) in which the pusher plate was not brought into contact with the ice, and F was therefore known to be zero. For the normal load cells, we were able to use the knowledge that we never applied a tensile (i.e. negative) normal load N, to identify a sudden drop with decreasing N in the frequency of occurrence of measurements, with zero normal load. For the shear-stress sensors, we identified those records where the ice was not being pushed (operationally defined as $|F| < 410N$) and was not moving (operationally defined as $|\dot{D}_j| < 330\mu\text{ms}^{-1}$) at times when the 9 shear stresses, τ_i, were zero. (The (i,j) pairs are those listed in figure 4.) We then used the least-squares method to fit a polynomial function of time to the apparent shear stress in these records, and took this function to be the offset. The order of polynomial to fit was chosen by undertaking, separately for each shear stress transducer, a series of significance tests for the departure from zero of each successive polynomial coefficient. The significance tests were based on the decomposition of the marginal likelihood (typical goodness of fit) of a model [31], into a best-fit likelihood factor and an "Occam factor" which encodes how finely the model has tuned itself to the data. The highest-order polynomial chosen by the significance tests was a cubic (for transducer pair $i = 6$). In all cases, the results presented below have had the inferred offsets removed, by subtracting them from the apparent measurements.

3 Results: Spatio-temporal properties of slip events

In figure 6a we show the spatial and temporal changes in shear stress during a single stick-slip event. The nominal air temperature was -7°C; the ice floe temperature profile measured during this test is shown in figure 2 (the warmer of the two temperature profiles). Fig. 6b is a two-dimensional shear stress-time slice through the 3D plot. Initial mean normal load was 57kN. The shear stress, τ_i, in the central ice floe is plotted as a series of shear stress sensor positions $i \in \{1, 2, 3, \ldots, 7\}$ along the fault against time. (The stress sensor at position 8 did not yield data.) Data were collected at 5000 samples per second and the full sampling frequency is used in the plot. Fig. 6a shows how high local shear stresses were initially induced at the pusher plate end of the ice floe and then propagated down the fault. The record at the first stress sensor position ($i = 1$) shows a gradually increasing shear stress with time, a peak stress, stress drop accompanying slip and then a return to a residual value. The strain pulse propagates in both space and time. There is a nucleation zone for slip covering the first two sensor positions ($i \in \{1, 2\}$), where the strain pulse is traveling slowly (at a minimum of 5.4 m.s^{-1}), followed by a propagation phase recorded at the sensor positions located along the fault (increasing distance x). The shear stress becomes impulsive (i.e., the wave-packet tends to a constant, narrow shape) traveling along the fault at speeds in excess of 56 m.s^{-1} (the highest we can measure). The speeds in the propagation phase are at least an order of magnitude higher than in the nucleation phase and we suspect will approach the Rayleigh wave speed in ice of

about 1.7 km.s^{-1} (Stamoulis and Dyer, 2000) [32]. This cycle of stick-slip events is then repeated (not shown) as the floes continue to be pushed past each other. Our preliminary analysis of the locations of acoustic emissions on the faults indicates that all cracking associated with frictional sliding was constrained to the faults. No cracking was observed perpendicular to the faults.

In figure 6c we use a schematic map to illustrate this behaviour where we have plotted the time to the stress drop against position on the ice floe. Figure 6 is a demonstration of nucleation zone in the frictional slip of ice. Shear stresses monitored along the length of the fault surface show how non-uniformly local shear stresses are induced and accumulated along the fault during increase of the shear load and how gradually the fault strength degrades in a localized zone prior to sliding. After the initiation phase, where the shear stress is increasing slowly, there is a propagation phase where the shear stress increases rapidly with time and distance down the fault. The slipping region behaves like a wave-packet, propagating away from the nucleation zone.

In figure 7 we show five pairs of variables from among the local shear stress, the slip displacement, the velocity and the acceleration of the central ice floe, recorded at one location, during a single stick-slip cycle. The style of presenting data from a single stick-slip cycle is modelled on that of Ohnaka et al. (1987) [33]. For the variation of local shear stress with slip displacement (Fig. 7a) we see that the shear stress rises to a peak at a small but non-zero amount of slip and then decreases to a residual shear stress with on-going slip displacement. The shear stress then starts to rise for the next stick-slip cycle. This is slip-weakening behaviour which has also been observed during stick-slip along pre-cut faults in rock [e.g., 33]. The slip-weakening failure energy can, in principle, be obtained from the plot of shear stress versus slip displacement in an analogous manner to rock. In figure 7b we see that the peak stress is attained at non-zero slip velocity. The slip velocity and acceleration are also plotted in figure 7 against displacement. Both accelerating and decelerating phases are clearly seen.

4 Mechanics of frictional slip

This paper focuses on frictional slip propagation during stick slip behaviour. Steady-sliding is also an important frictional phenomenon which has been the usual subject for experimental research and modelling. But it seems likely that stick-slip behaviour plays a significant role in pressure-ridge building in the polar pack as well as controlling floe-floe sliding. Stick-slip in ice is a second-order frictional phenomenon likely to be controlled by a complex interplay of mechanisms and promoted by increasing normal stress and decreasing temperature. However little research has been done on the mechanics [7, 25, 27]. In rock mechanics stick-slip is promoted by smooth surfaces indicating a strong dependence on the characteristic length of geometric irregularities on the fault surface [34].

The strong similarity with stick-slip behaviour in rock allows us to model qualitatively the constitutive behaviour of ice floe friction in an analogous manner. When the tip of the slipping zone propagates, the shear stress reaches a peak value at the tip, behind which is a “breakdown zone” where the stress drops to the residual frictional sliding stress levels. The breakdown zone size, D_{bd}, is equal to the nucleation zone size at the point where the rupture starts to propagate dynamically (Fig. 6). This has been observed during the high-resolution rock friction experiments of Ohnaka and feng-Shen (1999) [26]. However in their experiments, frictional slip nucleated at a zone of minimum shear strength. In our experiments, because of the relatively high homogeneity of saline ice compared to granite there was no strongly contrasting minimum shear strength. The area under the shear stress versus slip displacement curve (figure 7a) is the critical energy release or shear rupture energy, G_c, and D_c is the critical slip displacement required for the local shear stress to decrease from the breakdown strength, τ_{max}, to the residual sliding friction level, τ_{res}. (Using the terminology of [34], this is the breakdown stress drop, $\Delta\ \tau_{bd}$). A cycle of breakdown and re-

strengthening process of stick-slip can be seen in terms of the shear stress and slip velocity (see figure 7b). In Phase I the shear stress increases to a maximum with increasing slip velocity ($d\tau/dt > 0$ and $d^2D/dt^2 > 0$). After the maximum shear stress the shear strength degrades rapidly with increasing acceleration to a level where the slip velocity has a maximum value. This is Phase II, the accelerating phase ($d\tau/dt < 0$ and $d^2D/dt^2 > 0$). In Phase III the slip movement is stabilized by a subsequent decelerating phase ($d\tau/dt < 0$ and $d^2D/dt^2 \leq 0$). In Phase IV, there is a re-strengthening ($d\tau/dt > 0$ and $d^2D/dt^2 < 0$). In Phase V the slip motion is stopped ($d\tau/dt > 0$ and $dD/dt = 0$) and time-dependent re-strengthening occurs.

The shear rupture energy, G_c, is related to the constitutive parameters $\Delta\tau_{bd}$ and D_c [35],

$$G_c = \int_0^{D_c} \left[\tau\left(D\right) - \tau_{residual}\right] dD = \frac{1}{2}\Gamma\Delta\tau_{bd} D_c \qquad \text{(Eq. 1)}$$

where Γ is a dimensionless parameter dependent upon the specific form of the slip-dependent constitutive relation [36]. This is illustrated schematically in figure 8.

In earthquake mechanics it has been argued that while both the breakdown zone size, D_{bd}, and the critical slip displacement, D_c, increase in size with increasing scale, their ratio, D_c / D_{bd} is independent of size-scale and for quasi-static slip weakening may be estimated by

$$\frac{D_c}{D_{bd}} = \frac{4(1-\nu)}{\pi}\frac{\Delta\tau_{bd}}{G} \approx \frac{\Delta\tau_{bd}}{G} \qquad \text{(Eq. 2)}$$

where ν is Poisson's ratio and G is the shear modulus [33, 35]. For dynamic rupture the breakdown shear stress has to be scaled by rupture velocity. In rock mechanics and earthquake mechanics D_c / D_{bd} is of the order of 10^{-3}.

5 Micromechanical Constitutive Law

5.1 Development of the Model

Friction laws based on micro-mechanics have a common conceptual framework: pressing two pieces of dry material together brings them into direct contact, over some fraction f of the total area A of the facing surfaces; this fraction is determined by the deformation of the asperities under the normal load N. A shear stress $T_{asperity}$ is then necessary to fail these direct contacts, giving

$$\tau = f T_{asperity} \qquad \text{(Eq. 3)}$$

There are multiple mechanisms involved in friction. Therefore a constitutive relation which aims to be built from fundamental physical processes resulting from asperity contact will have many parameters. This contrasts with phenomenological laws such as Amontons's law or the rate and state friction laws which have just a few [25]. But while μ or the rate and state parameters need to be measured in experiments, the adjustable parameters in micromechanical friction laws could in principle (although not necessarily in practice) be directly measured, for instance in neutron diffraction experiments [1].

The deformation of asperities under the normal load may be either ductile [14] or elastic [24]. Shear failure of the interface may be either ductile or brittle, or for a material typically near its

melting point, such as ice, proceed by the melting of material by the heat dissipated by friction and Couette flow of the consequent fluid layer [37, 16]. For materials in general the assumption of ductile deformation under normal load, along with the assumption of constant $T_{asperity}$, has been used to reproduce the classic (originally phenomenological) Amontons's law, with the coefficient of friction μ independent of normal stress. The assumption of elastic deformation under normal load, again with constant $T_{asperity}$, produces a friction law dependent on surface topography, with a power law dependence of friction on normal stress [24]:

$$\tau \propto \sigma_n^{\,n} \qquad \text{(Eq. 4)}$$

For the case where all the asperities are the same height, $n = 2/3$. Various workers have repeated the analysis for other surface topographies and produced a variety of power-law dependencies of τ on σ_n between 2/3 and 1 [1].

Slip weakening, where shear stress degrades rapidly with slip displacement before reaching a near-constant value at large displacements, can be modelled by a slip weakening factor, w_s ,

$$w_s = 1 + M \exp\left(-D^H / D_0\right) \qquad \text{(Eq. 5)}$$

Physically this represents the effect of spatially non-uniform slip within an individual asperity contact [38]. D^H is the slip displacement (measured since sliding stopped in the previous stick-slip cycle). M and D_0 are adjustable parameters. D_0 is a characteristic displacement for an asperity contact, representing the displacement required to make sliding velocity homogeneous across the asperity. Note this contrasts with the critical slip displacement, D_c , which is the amount of displacement required for the shear stress to return to a residual level.

Lubricated (hydrodynamic) friction is where direct contact of the sliding surfaces is prevented by an intervening layer of fluid. The interfacial fluid may be generated through the frictional melting of ice at the interface [15, 16]. If the fluid layer is thick enough to behave in a laminar fashion then the shear stress is the ratio of the product of sliding velocity, dD/dt and fluid viscosity η to fluid layer thickness l,

$$\tau = \eta \dot{D} / l \qquad \text{(Eq. 6)}$$

Hatton et al. (2009) [1] revisited these standard approaches, taking account of the unusual mechanical properties of ice. These properties make several major differences to the resulting friction laws. 1) The stress in ductile deformation of sea ice is strain-rate-dependent, i.e., time-scale-dependent. For ductile deformation under normal load, the relevant time-scale is the length of time for which a typical contacting asperity has been in contact. This can be expressed in terms of the instantaneous sliding velocity, the instantaneous sliding acceleration, the typical length scale of an asperity along the sliding direction and introduces dependences on velocity and acceleration in the shear stress. For ductile shear failure of the interface, the strain rate is proportional to sliding velocity, again introducing velocity-dependence in the shear stress. 2) The stress-strain relationship in elastic deformation of ice is also time-scale dependent [39]; for elastic deformation under normal load, this again introduces velocity and acceleration dependences in the shear stress, albeit of a different form from those found for ductile deformation under normal load. 3) The brittle shear fracture stress of ice depends on the tensile longitudinal stress: the exponent in the power-law dependence of shear stress on normal stress is perturbed when the shear failure of the interface is brittle [40].

Hatton et al. (2009) [1] proposed to unify the models for the response to normal load and the shear failure of the real contact, by a principle of maximum displacement for normal deformation, and of minimum stress for shear failure:

$$\tau = max\ (f_{el}, f_{du})\ smallest(T_{du}, T_{br}, T_{ml}). \qquad \text{(Eq. 7)}$$

That is, they pick the largest value for real contact fraction (elastic f_{el} or ductile f_{du}) and the smallest value for shear strength (ductile T_{du}, brittle T_{br} or melting lubrication, T_{ml}).

This unified model contains four adjustable parameters, dimensionless melt-water expulsion displacement X, the dimensionless contact-breaking displacement Y, the dimensionless shear layer thickness Z and the typical normal asperity strain ε_* (see figure 9). The predictions from this model have been presented by Hatton et al. (2009) [1]. (An alternative model has been proposed [17] for a melting-lubrication model for rocks which could be applied to ice.)

Quantitatively, the melting-lubrication model predicts a shear strength:

$$T_{ml} = \frac{sgn\dot{D}}{\pi^{1/4}(XR_c)^{1/2}} \left[\left[(\kappa c \rho_s)^{1/2} (\Theta_m - \Theta) / \left|\dot{D}\right|^{1/2} \right] + \left[(\kappa c \rho_s)(\Theta_m - \Theta)^2 / \left|\dot{D}\right| + 2\eta L \rho_l \left|\dot{D}\right| \right]^{1/2} \right] \qquad \text{(Eq. 8)}$$

where κ is the thermal conductivity of ice, c is the specific heat capacity of ice, ϱ_s is the density of ice, η is the viscosity of water, L is the specific latent heat of melting of ice, and ϱ_l is the density of the brine (Table 1). Θ is temperature and Θ_m is the melting temperature which is pressure-dependent [1].

X is the typical distance the ice floe has to move between a fluid element being generated by melting, at the leading edge of an individual asperity contact and the fluid element being ejected at the trailing edge of the asperity contact (Fig. 9). X was a topographic property of our particular sample; its involvement in this model, but not its value, is established by Oksanen and Keinonen (1982) [16]. Therefore, we treat X as an adjustable parameter. Equation 8 has two interesting properties. The first is that there is competition between terms in the interface failure stress $T_{asperity}$, involving the conduction of heat away from the fault, which decrease with increasing velocity, and terms involving melting and viscous dissipation, which increase with increasing velocity. The second is that the normal-load dependence of the pressure melting will convert the pure power-law normal-load dependence into multiple power-law regimes with different exponents which is inherited from the contact fraction f.

Models of the contact fraction f are based on elastic or plastic deformation under the normal load of a variety of surface topographies. The theoretical model for a two-stage "fractal" distribution of peak heights, by which is meant a population of identical, hemispherical asperities, on whose surfaces is another population of smaller, identical hemispherical asperities, on whose surfaces in turn is a third population of still smaller identical asperities [24]. In reality, it does not matter whether the asperities are configured in exactly this fashion: all that is important is that the frequency density distribution of peak heights is the same as if they were distributed this way. Hatton et al (2009) [1] give the real contact fraction for elastic deformation under normal load to be:

$$f_{el} = \frac{3^{41/9} \pi^{35/27} {P_C}^{1/3} {R_C}^{2/3} N^{26/27}}{2^{148/27} \times 13 E'^{26/27}} \sigma^{26/27}$$

(Eq. 9)

The asperity topography is shown schematically in Fig. 9. P_C represents the total number of asperity peaks per unit area on the surfaces and R_C represents the radius of curvature of a typical asperity peak for the smallest-scale of the three asperity populations, and P_B the total number of asperity peaks per unit area on the surfaces and R_B represents the radius of curvature of a typical asperity peak for the medium-scale of the three asperity populations, d_G represents the ice grain size and Y represents the length of a typical individual asperity contact. Y is an adjustable parameter. E' is the adjusted Young's Modulus. The parameters are topographic properties of our particular sample. Their values were measured to be: P_c = 5.53/mm^2, and the typical radius of curvature of a peak, R_C = 160 μm.

The real contact area for ductile deformation under normal load is:

$$f_{du} = \left(\frac{A}{\dot{\varepsilon}_n}\right)^{1/n} exp\left(-\frac{Q}{nR\Theta}\right)\sigma \qquad \text{(Eq. 10)}$$

where Q is an activation energy for the delayed elastic strain and R is the molar gas constant. (See Table 1.)

The time for which a typical individual asperity contact has existed, t^H, is [1]:

$$t^H = \frac{\dot{D} \pm \sqrt{\dot{D}^2 \pm 2Y\ddot{D}}}{\ddot{D}} \qquad \text{(Eq. 11)}$$

The contact fraction $f_{fractal}$, the shear strength T_{ml} and the slip-weakening factor w_s can be combined to produce a theoretical expression for the shear stress required for sliding:

$$\tau = f_{fractal}\, T_{ml}\, w_s \qquad \text{(Eq. 12)}$$

The total number of adjustable parameters is seven which we expect to be capable of estimating their values with reasonable precision.

5.2 Fitting experimental data to the micromechanical model

Our data set, from multiple stick-slip events from 22 experimental runs, is of the order of 100 million data points. From the point of view of testing a frictional constitutive law it is useful to plot shear stress against slip displacement, velocity and normal load, while the other variables are held constant.

Figure 10 shows where the dependent variable, shear stress τ_i in the central floe, is plotted against: a) the slip displacement of the central ice floe, D_f^H, since the last time it stopped, plotted on a log scale to show the behaviour at low slip; b) the velocity and d) the normal load N. In Fig. 10c the coefficient of friction, τ_i A/N, is plotted against normal load. The data are from all 22 experiments done over a range of normal stresses, temperatures, hold times and speeds, representing many hundred of individual stick slip events. In each plot, constant values of the four independent variables not displayed (i.e., four out of displacement, velocity, acceleration, normal load and

temperature) are simulated by selecting for inclusion only those samples where the four variables were within specified narrow ranges. There is no plot of shear stress against temperature as the control ranges used for the extraneous variables are so tight that once displacement, velocity, acceleration and normal load are controlled, all the half-dozen or so measurements that remain are at the same temperature. The mechanical and topographic properties input are from the measured surface profiles and grain size (Table 1). The adjustable parameter values used are $X = 0.054$; $Y = 0.025$; $Z = 0.20$; $\varepsilon_* = 0.124$; $M = 6$; and $D_0/R_C = 3.08$.

The data are somewhat noisy but that does not prevent lineations being visible in the plots or formal statistical testing of friction laws. The first lineation is in the shear stress against displacement graph (Fig.10a), where the shear stress rapidly decreases with increasing displacement, before reaching a near-constant value at large displacement. This militates in favour of the idea that displacement-independent friction laws are large-displacement, equilibrium limits. To model this we introduce the slip-weakening factor (Equation 5). In the shear stress against velocity plot (Fig. 10b) there is a sharp fall at low velocity in the theoretical model, below which data are present. (This is what constrains the Y parameter in the theoretical model to be small.) It represents a transition (with decreasing velocity) to melting and lubrication, with heat supplied by conduction from the bulk of the ice. At the very high-velocity end, a kink represents a transition (with increasing velocity) to melting and lubrication, this time with the heat supplied by frictional dissipation. In Fig. 10c the coefficient of friction is plotted against normal load. The exponent for the theoretical-model is zero. The rate and state family of models [e.g., 23, 25] generally share the zero exponent predicted by the Hatton et al. model. The data in figure 10c appear to have a non-zero, negative exponent. This is a surprising feature of the data, because no current theoretical model can reproduce it. In Fig. 10d the shear stress is plotted against normal load. This appears to follow a straight line on these logarithmic axes, which indicates a power-law dependence but with an exponent close to 1. Theoretical models involving elastic deformation under the normal load produce power laws for the shear stress as a function of normal load with exponents ranging between 2/3 and 1, depending on the surface topography. There is no plot of shear stress against acceleration as there was no clear lineation.

In Figs. 10a, 10c and 10d the smallest shear stress algorithm for the shear failure mechanism chooses brittle shear fracture throughout. It also chooses brittle shear fracture in the middle-velocity section of the top Fig. 10b. At higher velocities, the theoretical model that is favoured by our experimental data involves failure of the interface through frictional heating, surface melting and hydrodynamic lubrication (equation 8).

6 Discussion

6.1 Stick-slip behaviour and slip wave propagation

The stick-slip behaviour illustrated in Figures 6-8 is highly reminiscent of the nucleation and propagation of a wave-packet, the order parameter that fluctuates in the wave-packet being sliding velocity: in a "nucleation zone," within ~1.5m of the pusher plate, the shear stress on the fault builds, along with the flexural strain in the pusher plate. This shear stress resists the load from the pusher plate, keeping the ice stationary. It also shields the rest of the fault from the effects of the pusher plate, keeping the shear stress outside the nucleation zone low. The nucleation zone becomes a zone of greatest shear stress. Eventually this shear stress becomes so great that the fault can no longer sustain it and the ice in the nucleation zone begins sliding, allowing the flexural strain in the pusher plate to relax and thereby unloading the ice. As the nucleation zone slides, the section of

fault at the boundary of the nucleation zone is subject to a rapidly increasing shear stress, because the ice behind it is moving forward, pushing on it, while the ice in front of it remains stationary (in other words, the time- derivative of shear stress is proportional to the spatial derivative of velocity). The slipping region (wave-packet) then propagates along the fault; when it reaches the end of the ice, the ice returns to rest, and the cycle begins again. In a sense, this wave-like behaviour is not surprising as the time-derivative of shear stress is proportional to the spatial derivative of velocity. Friction laws discussed earlier relate shear stress to velocity, creating a relationship between the spatial derivative of velocity and the time-derivative of velocity, i.e., a wave equation for the velocity.

There is evidence for this occurring in the central Arctic sea ice pack from the SIMI experiment of 1994. Stamoulis and Dyer (2000) [32] analyzed hydrophone records of seismic waves radiated by fractures to estimate fracture velocity. They measured velocities from less than 100 $m.s^{-1}$ to 1100 ms^{-1}: well below the Rayleigh wave velocity of 1700 $m.s^{-1}$, which should bound the velocity of propagation of shear cracks in ice. These measurements are consisted with our proposal for nucleation and propagation phases for shear rupture in sea ice.

From Fig. 7 we can see that the breakdown zone size, D_{bd} , is approximately 1.5m long. Typical critical slip displacements, D_c , (Fig. 7a and 8a) are about 3mm. Therefore the ratio, ε_c , is about 2 x 10^{-3}. This is roughly the ratio found in rock and earthquake mechanics [26] and seems to suggest that we could expect this ratio to be scale independent. From Fig. 7 the breakdown shear stress, $\Delta\tau_{bd}$, is approximately 40kPa. The shear modulus of saline ice, G, is about 2.9 GPa [41]. So their ratio is about 10^{-5}. In our experiments we are propagating rupture at low normal stresses and low shear stresses. Ohnaka et al. (1987) [33] note that in rock mechanics ε_c ranges from 10^{-5} to 10^{-3}, depending on normal stress. So again this is within the expected range. The shear rupture energy, G_c (Equation 1), is approximately 13 kJm^{-2} for the test shown in Fig. 7. By comparison, small-scale stick-slip experiments in rock mechanics give shear rupture energies of about 1 Jm^{-2} and major earthquakes values of 10^6 to 10^8 Jm^{-2} [26]. This illustrates the strong control the critical slip displacement has on shear rupture energy and opens up a fracture mechanics approach to modelling the arctic sea ice cover.

6.2 Constitutive law for sea ice friction

We employed a friction law that can be incorporated into geophysical-scale sea ice rheological models, when coupled with a fault population model [13]. The data are used to constrain the values of parameters within the Hatton et al. (2009) model[1], not for testing of the correctness of the model itself. Physically, this law, for our test conditions with stick-slip behaviour, represents a situation for ductile deformation under normal stress conditions throughout. The shear failure mechanism is through brittle failure of asperities with a transition, at the very high-velocity end, to melting and lubrication. The heat is supplied by frictional dissipation. Acoustic emissions measured during the sliding indicate brittle fracture of asperities is occurring. There is also wear on the sliding surface. Interestingly, in achieving this global fit, the parameter estimation algorithm has not placed the minimum of shear stress with respect to velocity in the location where our visual inspection of the data suggested that it may be, nor has it placed a change in exponent of the shear stress as a function of normal load, in the location where we tentatively identified a step-like feature in visual inspection, nor indeed has it chosen a characteristic displacement length scale D_0 as long as we might have estimated by visual inspection. In all three cases, it has found the overall magnitude of the shear stress to be a more important consideration in choosing parameters than the location of these second-order features. It is also interesting that we find ductile deformation of asperities under normal stress to be the appropriate mechanism.

The ice sliding surface had a measured fractal distribution of asperity heights. (Archard (1957) [24] proposed a fractal asperity distribution before the term fractal was coined.) There are three radii of curvature involved in the topography: R_C (small asperities), R_B (medium asperities) and R_A (large asperities). However, only small asperities (R_C) and medium asperities (R_B) are involved in the friction law. Physically, increasing R_A brings more medium asperities on any one large asperity into contact, but also increases the total number of medium asperities on the large asperity, so that the fraction of the medium asperities that are in contact stays constant. In addition, increasing R_A increases the load on, and therefore the contact area, of medium asperities at any given distance from the large asperity centre. But increasing R_A also brings into contact medium asperities further out from the large- asperity centre, so that the typical area contributed by a contacting medium asperity stays constant. Overall, the value of increasing R_A has no effect on the mechanics.

Many aspects of the data are captured by the model of Hatton et al. [1]. We do not have a full set of predictions from any other model against which to benchmark. For comparison of the theoretical model for stable sliding behaviour, where we do not have experimental data, we plot (Fig. 11) the coefficient of kinetic friction as a function of sliding velocity for the experimental data of Schulson and Fortt [23] and Maeno and Arakawa and data therein[41]. This plot is for granular ice, of grain size 1mm, at temperature 263K and at those velocity conditions sliding is steady, not stick-slip, form. These data are presented [23, 41] in a time-averaged way, which means that only the smooth-sliding subsets are relevant for comparison with the predictions from the theoretical model of Hatton et al. [1]. These subsets of their data are shown as points with error bars. The theoretical model [1] is shown as a line. The mechanical and topographic properties are given in Table 1 and with grain size of 1mm, temperature 263 K, and acceleration 10^{-11} ms^{-2}. The coefficient of kinetic friction has been taken as the average gradient of shear stress with respect to normal stress, for normal stresses between 20 kPa and 70 kPa. The adjustable parameters in the theoretical model of Hatton et al. [1] have been set by Levenberg-Marquardt least-squares fitting to the experimental data and are: X = 0.010; Y = 0.81; Z = 0.9921; and $\varepsilon^\star = 0.40$. Physically, the theoretical model predicts that throughout, deformation under the normal stress is ductile, with the local normal stress at the contacting asperity tips being in a fixed ratio to the Glen's-law yield stress. Therefore, as a result of the rate-dependence in Glen's law, the local normal stress at the contacting asperity tips increases with increasing velocity. At the left-hand, low-velocity end of Fig. 11, this variation in local normal stress means that the melting temperature at the asperity tips decreases with increasing velocity, along the ice Ih liquidus. Also at the left-hand, low-velocity end, the shear failure mechanism is ductile deformation under shear. The local shear stress required to produce ductile shear failure of the contacting asperities increases with increasing normal stress (and therefore with increasing velocity) according to Glen's law, i.e. as a power law with the same exponent as the local normal stress at the contacting asperities. The local shear stress required to produce brittle shear failure of the contacting asperities also increases as a power law with increasing velocity, according to the law discovered by Rist and Murrell [40]; however, the exponent in this power law is smaller than that for the ductile shear failure by a factor of 0.67. Therefore, as the velocity increases, it reaches a point, around 1.3×10^{-5} ms^{-1}, beyond which the brittle shear failure stress of the contacting asperities is less than their ductile shear failure stress, and brittle fracture becomes the dominant shear failure mechanism of the contacting asperities. When the velocity reaches about 3×10^{-4} ms^{-1}, the contacting asperity tips reach the ice Ih/ice III eutectic. Beyond this point, the melting temperature at the asperity tips increases with increasing velocity, along the ice III liquidus. As the velocity increases further, it reaches a point, around 10^{-4} ms^{-1}, where the melting temperature at the contacting asperity tips is equal to the bulk temperature of the ice, and the asperity tips can be melted by heat conducted in from the bulk of the ice, without any need for heat generation from frictional dissipation. Once this happens, shear failure by melting and lubrication becomes dramatically easier - so that melting-lubrication becomes shear failure mechanism, and the sliding shear stress drops to a negligible value. As the velocity increases further, it reaches a point, around

1.3×10^{-3} ms^{-1}, where the melting temperature at the asperity tips is equal to the bulk temperature of the ice, and the asperity tips can no longer be melted by heat conducted in from the bulk of the ice - beyond this point, melting requires frictional dissipation. Once this happens, shear failure by melting and lubrication becomes dramatically more difficult - so that brittle shear fracture once again becomes the shear failure mechanism, and the sliding shear stress is no longer negligible.

7. Conclusion

We have presented results from frictional sliding experiments on floating saline ice floes in the HSVA ice tank. These experiments broadly simulate conditions of temperature, strain rate and shear stress found in the high Arctic Ocean. We found that frictional slip is predominantly by quasi-cyclic stick-slip behaviour. A stick-slip cycle takes the form of repeated nucleation near the pusher plate and propagation along the fault of spatially and temporally localized wave-packets in the sliding-velocity field. The ice-ice friction law is characterized by slip-weakening, i.e., by a frictional shear stress that decreases with increasing sliding displacement for small positive sliding displacements, then reaches a near-constant value for larger sliding displacements. We have followed the theoretical model development of Hatton at al. (2006) [1] to fit the experimental data. The constitutive law for lubricated friction of sea ice floes follows Archard's law rather than Amontons's law, with $\tau \propto \sigma_n{}^n$, with $n = 26/27$. The surface asperities deform elastically under normal load but the interface fails in shear through a process of frictional heating, localized surface melting and hydrodynamic lubrication.

We therefore propose, for inclusion in geophysical-scale sea ice models, the single-fault shear-stress friction law, fractal asperity height distribution, melting lubrication and slip weakening model:

$$\tau = f_{fractal}\, T_{ml}\, w_s$$

with the following values for the adjustable parameters of the law: $X = 5.3\ \mu$m, $Y = 44.1\mu$m, $P_C R_C{}^2 = 2.83 \times 10^{-13}$, $P_B R_B{}^2 = 1.42$ x10^{-3}, $d_G = 6.9$mm, $D_0 = 36.9\mu$m and $M = 0.125$.

Additional Information

Acknowledgments

We thank the Hamburg Ship Model Basin (HSVA), especially the ice tank crew, for the hospitality and technical support and Richard Rabe, Steve Boon, John Bowles, and Neil Hughes at UCL for engineering support. We thank Ben Lishman for helpful discussions. DLF and DCH acknowledge financial support made available from the Leverhulme Trust. DCH acknowledges financial support from Rio Tinto.

Funding Statement

This research was funded by the UK Natural Environment Research Council. Access to the Research Infrastructure ARCTECLAB was financially supported within the 5th Framework Programme by the Improving Human Potential Programme from the European Union through contract HPRI-CT-2001-00126.

Competing Interests

We have no competing interests.

Authors' Contributions
Sammonds conceived the experiments. Hatton analysed the data. Hatton, Sammonds and Feltham executed the experiments, interpreted the data and wrote the article.

References

1. Hatton, D.C, Sammonds, P.R. & Feltham, D.L. 2009 Ice internal friction: Standard theoretical perspectives on friction codified, adapted for the unusual rheology of ice, and unified. *Philos. Mag.*, **89**(31), 2771–2799. doi: 10.1080/14786430903113769.

2. Seymour-Pierce, A., Lishman, B. & Sammonds, P. 2016 Recrystallisation and damage of ice in winter sports, *this volume*.

3. Scourfield, S., Sammonds. P., Lishman, L. & Marchenko, M. 2015 The effect of ice rubble on ice-ice sliding, In: Proc 23rd Int. Conf. Port & Ocean Engineering under Arctic Conditions June 14-18, 2015 Trondheim, Norway.

4. McCarthy, C., Savage, H., & Nettles. M. 2016 Temperature dependence of ice-on-rock friction at realistic glacier conditions, *this volume*.

5. Weiss, J. & Dansereau, V. 2016 Linking scales in sea ice mechanics, *this volume*.

6. Middleton, C.A., Grindrod, P.M. & Sammonds, P.R. 2016 The effect of rock particles and D2O replacement on the flow behaviour of ice, *this volume*.

7. Sammonds, P.R., Murrell, S.A.F. & Rist, M.A. 1998 Fracture of multiyear sea ice. *J. Geophys. Res.*, **103**(C10), 21795–21815.

8. Kwok. R. 2001 Deformation of the Arctic Ocean sea ice cover between November 1996 and April 1997: A qualitative survey. In Dempsey, J.P. & Shen, H.H. 2001 *Scaling Laws in Ice Mechanics and Ice Dynamics*, pp. 315–322, Kluver, Amsterdam.

9. Marko, J.R. & Thomson, R.E. 1977 Rectilinear leads and internal motions in the ice pack of the western arctic ocean. *J. Geophys. Res.*, **82** (C6), 979–987.

10. Hopkins, M.A., Tuhkuri, J. & Lensu. M. 1999. Rafting and ridging of thin ice sheets. *J. Geophys. Res.*, **104** (C13), 13605–13613. doi: 10.1029/1999JC900031.

11. Tuhkuri J. & Lensu. M. 2002 Laboratory tests on ridging and rafting of ice sheets. J. *Geophys. Res.*, **107** (C9), 3125. doi: 10.1029/2001JC000848.

12. Sammonds, P.R. & Rist, M.A. 2001 Sea ice fracture and friction. In Dempsey, J.P. & Shen, H.H. 2001 *Scaling Laws in Ice Mechanics and Ice Dynamics*, pp. 183-194.

13. Taylor, P.D., Feltham, D.L., Sammonds, P.R. & Hatton. D.C. 2006 Continuum sea ice rheology determined from subcontinuum mechanics. *J. Geophys. Res.*, **111** (C11), C11015–1–C11015–14. doi: 10.1029/2005JC002996.

14. Bowden, F.P. & Tabor, D. 1967 *Friction and Lubrication*. Metheun & Company, London.

15. Evans, D.C.B., Nye, J.F. & Cheeseman, K.J. 1976 The kinetic friction of ice. *Proc. R. Soc. Lond. A*, **347**, 493–512.

16. Oksanen, P. & Keinonen, J. 1982 The mechanism of friction of ice. *Wear*, **78**, 315–324.

17. Nielsen, S., Di Toro, G., Hirose, T. & Shimamoto, T. 2008. Frictional melt and seismic slip. *J. Geophys. Res.* **113**, B01308. doi:10.1029/2007JB005122.

18. Persson, B.N.J. 2015. Ice friction: Role of non-uniform frictional heating and ice premelting. *J. Chemical Physics* **143**, 224701.

19. Rist. M.A. 1997 High-stress ice fracture and friction. *J. Phys. Chem. B,* **101**(32); 6263–6266. doi: 10.1021/jp963175x.

20. Barnes, P., Tabor, D. & Walker. J.C.F. 1971 The friction and creep of polycrystalline ice. *Proc. R. Soc. Lond. A*, **324** (1557), 127–155.

21. Kennedy, F.E., Schulson, E.M. & Jones, D.E. 2000 The friction of ice on ice at low sliding velocities. *Philos. Mag. A,* **80**(5), 1093–1110. doi: 10.1080/01418610008212103.

22. Maeno, N.M., Arakawa, A., Yasutome, A. & Kanazawa, S. 2003 Ice-ice friction measurements, and water lubrication and adhesion-shear mechanisms. *Can. J. Phys.*, **81**, 241–249.

23. Schulson, E. M. & Fortt, A.L. 2012 Friction of ice on ice, *J. Geophys. Res.*, **117**, B12204, doi: 10.1029/2012JB009219.

24. Archard. J.F. 1957 Elastic deformation and the laws of friction. *Proc. R. Soc. Lond. A*, **243**(1233), 190–205.

25. Lishman, B., Sammonds, P.R. & Feltham, D.L. 2011 A rate and state friction law for saline ice. *J. Geophys. Res.*, **116** (C05), C05011–1–C05011–13. doi: 10.1029/2010JC006334.

26. Ohnaka, M. & feng-Shen, L. 1999 Scaling of the shear rupture process from nucleation to dynamic propagation: Implications of geometric irregularity of the rupturing surfaces. *J. Geophys. Res.*, **104** (B1), 817–844.

27. Lishman, B., Sammonds, P.R. & Feltham, D.L. 2013 Critical slip and time dependence in sea ice friction. *Cold Reg. Sci. Tech.*, **90-91**, 9–13. doi: 10.1016/j.coldregions.2013.03.004.

28. Sammonds, P.R., Hatton, D.C., Feltham, D.L. & Taylor. P.D. 2005 Experimental study of sliding friction and stick-slip on faults in floating ice sheets. In Proc. 18th Int. Conf. Port and Ocean Engineering Under Arctic Conditions, vol. 1, pp. 303–312, Potsdam, New York, June 29 2005. Clarkson University, Clarkson University.

29. Duckworth, R. & Westerman, P.H. 1989 Stress and strain instruments developed for field measurements of ice. *IEEE J. Ocean. Eng.*, **14** (2), 159–165. doi: 10.1109/48.16829.

30. Scott, D.R., C. J. Marone, C.J. & C. G. Sammis, C.G. 1994 The apparent friction of granular fault gouge in sheared layers, *J. Geophys. Res.* 99 7231.

31. MacKay, D.J.C. 1992. Bayesian interpolation. *Neural Comput.*, **4**(3), 415–447. doi: 10.1162/neco.1992.4.3.415.

32. Stamoulis, C. & Dyer. T. 2000 Acoustically derived ice-fracture velocity in central Arctic pack ice. *J. Acoust. Soc. Am.*, **108,** 96–104.

33. Ohnaka, M., Kuwahara, Y. & Yamamoto, K. 1987 Constitutive relations between dynamic physical parameters near a tip of the propagating slip zone during stick-slip shear failure. *Tectonophysics*, **144,** 109–125.

34. Sammonds, P. R. & Ohnaka, M. 1998. Evolution of microseismicity during frictional sliding, *Geophys. Res. Letts.*, **25**, 699-702.

35. Rice. J.R. 1980 The mechanics of earthquake rupture. In Dziewonski A.M. & Boschi, E. eds., *Physics of the Earth's Interior*, pp. 555–649. North-Holland, New York.

36. Ohnaka, M. & Yamashita, T. 1989 A cohesive zone model for dynamic shear faulting based on experimentally inferred constitutive relation and strong motion source parameters. *J. Geophys. Res.*, **94** (B4), 4089–4104.

37. Bowden, F. P. & Hughes, T.P. 1939 The mechanism of sliding on ice and snow, *Proc. Roy. Soc. Lond. A Mat.*, **172**(949), 280–298.

38. Yoshioka, N. & Iwasa, K. 1996 The characteristic displacement in rate and state- dependent friction from a micromechanical point of view, *PAGEOPH*, **147**, 433-453.

39. Sinha, N.K. 1978 Rheology of columnar-grained ice, *Exp. Mech.*, pp. 464–470.

40. Rist, M.A. & Murrell, S.A.F 1994 Ice triaxial deformation and failure, *J. Glaciol.*, **40**(135), 305–318.

41. Maeno, N. & Arakawa, M. 2004 Adhesion shear theory of ice friction at low sliding velocities, combined with ice sintering, *J. Appl. Phys.*, **95**(1), 134-139.

Figure and table caption

Table 1
Table of variable and parameters used in the micromechanical models (see Hatton et al, (2009) [1]).

Table 2
Table of experiments.

Figure 1
Photograph of the HSVA Arctic Environmental Test Basin showing our experimental set-up for a lubricated double-direct-shear test on floating saline ice floes. The bridge across the basin is used to push a central block of ice between two side blocks which apply a normal load, provided by side pusher panels (bottom left). The basin is 30 m long by 6 m wide. This is shown schematically in figure 4.

Figure 2
Temperature profiles of the middle of the ice sheet are shown for two experiments discussed in the text done on Day 1 (Temp T1) and Day 2 (Temp T2) of the test program. The nominal air temperatures were −7°C and −6°C respectively.

Figure 3
a) Pair of vertical thin sections taken through the thickness of the ice sheet and two horizontal thin sections taken at 15 mm depth (top) and 90 mm depth in the plane of the ice sheet, viewed under crossed polarizing lenses. The grid size is 10 mm × 10 mm. (See Hatton et al. (2009, Fig. 9 and supplementary online material B [1]). b) Profile of a replica surface and asperity height distribution taken from the frictional sliding surface. The direction of sliding is x and z is the vertical direction in the ice sheet. The area of the surface sampled is 10mm by 10mm.

Figure 4
Schematic diagram of the double-direct shear test in the HSVA environmental test basin. R1 to R8 denote the positions of 8 pairs of stress sensors mounted as two limbs of rosettes which measured local shear stresses. 6 transverse displacement transducers mounted at 1m intervals measured local normal displacement. D1 to D8 denote the position of 8 longitudinal displacement transducers, mounted to measure slip displacement. 8 acoustic transducers (not shown) recorded acoustic emissions.

Figure 5
The shear stress τ_4 in the central ice floe, during a single stick-slip event in experiment number 1-4, is plotted, as points, against the displacement D_2; the subscripts "4" and "2" index the positions along the fault where the shear stress sensor and displacement were measured; these are roughly equivalent positions (see Fig 4). Data were collected at 5000 samples per second, and the full sampling frequency is used in this plot. $D_{(start-0)}$ is an arbitrary origin for displacement.

Figure 6
a and b. The shear stress τ_i in the central ice floe, during a single stick-slip event in experiment number 2-8, is plotted, as points, against the position x where the shear stress sensor was positioned and the time t; the subscript "i" indexes the position x. Data were collected at 5000 samples per second, and the full sampling frequency is used in this plot.

c. Schematic map of the processes taking place on the fault, as a function of position and time.

Figure 7
Five pairs of variables, from among the shear stress τ_4 in the central ice sheet, the displacement D_2 of the central ice sheet, the velocity $\dot{D}_2$ of the central ice sheet, and the acceleration 2 of the central ice sheet, during a single stick-slip event in experiment 1-4, are plotted, as points; the subscripts "4" and "2" index the positions along the fault where the shear stress sensor and displacement were measured; these are roughly equivalent positions (see figure 4). $D_{2(start-1)}$ is an arbitrary origin for displacement.
a) Shear stress is plotted against displacement. b) Shear stress is plotted against velocity. c) Velocity is plotted against displacement. d) Acceleration is plotted against displacement. e) Shear stress is plotted against acceleration.

Figure 8
Schematic diagram (from figure 7). The behaviour shows an initial Phase I where peak shear stress is attained, an accelerating Phase II, a decelerating Phase III, a re-strengthening Phase IV, and in Phase V a time dependent strengthening.

Figure 9
Lubricated sliding asperity contact model. Two levels of asperities are shown (medium and smaller size, with radii of curvature, R_B and R_C respectively). Melt is generated at the contact and expelled. X is the distance the ice floe has to slide between a fluid element being generated by melting at the leading edge of an individual asperity contact and being expelled at the trailing edge. D_0 is a characteristic displacement representing the slip required for complete replacement of the real asperity contact area. Y is the contact destruction length representing the typical individual asperity contact during sliding.

Figure 10
The dependent variable, shear stress τ_i, in the central ice, during all the HSVA Hamburg experiments, is plotted. Top left a: shear stress is plotted against displacement. Top right b: shear stress is plotted against velocity. Bottom left c: coefficient of friction is plotted against normal load. Bottom right d: shear stress is plotted against normal load.

Figure 11
Comparison of the experimental data of Schulson and Fortt [23] (shown as points with error bars) with predictions from the theoretical model [1] (line). The coefficient of kinetic friction is plotted as a function of sliding velocity.

Table 1

Symbol		
Measured variables		See [1]
N	Normal load	
σ_n	Normal stress	
τ	Shear stress	
$\Delta\tau_{bd}$	Breakdown stress drop	
D	Slip displacement	
D^H	Slip displacement since previous cycle	
D_c	Critical slip displacement	
Θ	Temperature	
Calculated variables		
G_c	Shear fracture energy	
f	Asperity contact fraction	
$f_{fractal}$	Fractal asperity contact fraction	
T	Shear strength of asperity	
T_{ml}	Shear strength of asperity (melting-lub)	
t^H	Asperity contact time	
w_s	Slip weakening parameter	
Fixed parameters		
R	Molar gas constant	8.31 J/(mol K)
A	Glen's law coefficient	3.56×10^{-12} / Pa^n s
n	Glen's law exponent	3
Q	Activation energy	65.7 kJ/ mol
E	Young's Modulus	9.3 GPa
G	Shear modulus	2.9 GPa
d_0	Elastic grain size scale	9 mm
t_0	Elastic relaxation time	199 ps
κ	Ice thermal conductivity	2.3 W/(mK)
c	Ice specific heat capacity	2.10 kJ/(kg K)
ρ_s	Ice density	920 kg/m^3
ρ_l	Liquid brine density	1.03 t/m^3
η	Water dynamic viscosity	1.79 mPa s
L	Specific latent heat of melting	333 kJ/ kg
Temperature and pressure dependent parameters		
Θ_m	Melting temperature	271.5 K
v	Poisson's ratio	0.34
Topographic properties of test ice		
P_c	Areal density of asperities	5.53×10^6/ m^2
R_c	Typical asperity radius of curvature	160 μm
d_G	Average grain size	9 mm
Adjustable parameters		
D_0	Characteristic slip displacement	Adjustable
M	Slip weakening parameter	Adjustable
X	Sliding distance for water expulsion	Adjustable
Y	Sliding distance to break contact	Adjustable
Z	Shearing layer thickness	Adjustable
$\underline{\varepsilon}$	Typical contact strain	Adjustable

Table 2

Table 2

Test no	Comment	Air temp	Side press	Nominal speed	Hold time	Comment
		C	bar	$mm.s^{-1}$	min	
1-1	Trial run	-7	n/a	n/a	n/a	No movement
1-2	Const speed	-7	0	7	0	Stick-slip
1-3	Const speed	-7	0	0.7	0	Stick-slip
1-4	Const speed	-7	0	2.1	0	Stick-slip
1-5	Const speed	-7	0	0.21	0	Stick-slip
2-1	Trial run	-6	n/a	n/a	n/a	No movement
2-2	Speed test	-6	2	0.21, 2.1, 0.7, 7	0	Stick-slip
2-3	Speed test	-6	2	0.21, 2.1, 0.7, 7	0	Stick-slip
2-4	Trial run	-6	2	n/a	n/a	No movement
2-5	Speed trial	-6	2	7, 0.7, 2.1, 0.21	0	Stick-slip
2-6	Side load test	-6	0, 1.5, 3	2.1	0	Stick-slip
2-7	Hold time test	-6	2	2.1	3, 9	Stick-slip
2-8	Hold time test	-6	2	2.1	30	Stick-slip
3-1	Side load test	-11	0, 1.5, 1.75, 3	0.21	0	Stick-slip
3-2	Hold time test	-11	1.75	0.21	5	Stick-slip
3-3	Hold time test	-11	1.75	0.21	30	No movement
3-4	Hold time test	-11	0	0.21	30	No movement
3-5	Trial	-11	0	0.21	0	Fault re-cut
3-6	Speed trial	-11	0	7, 0.7, 2.1, 0.21	0	Stick-slip
3-7	Speed trial	-11	1	7, 0.7, 2.1, 0.21	0	Stick-slip
3-8	Const speed	-11	0	7	0	Stick-slip
3-9	Const speed	-11	0	7	0	Stick-slip

Figure 1

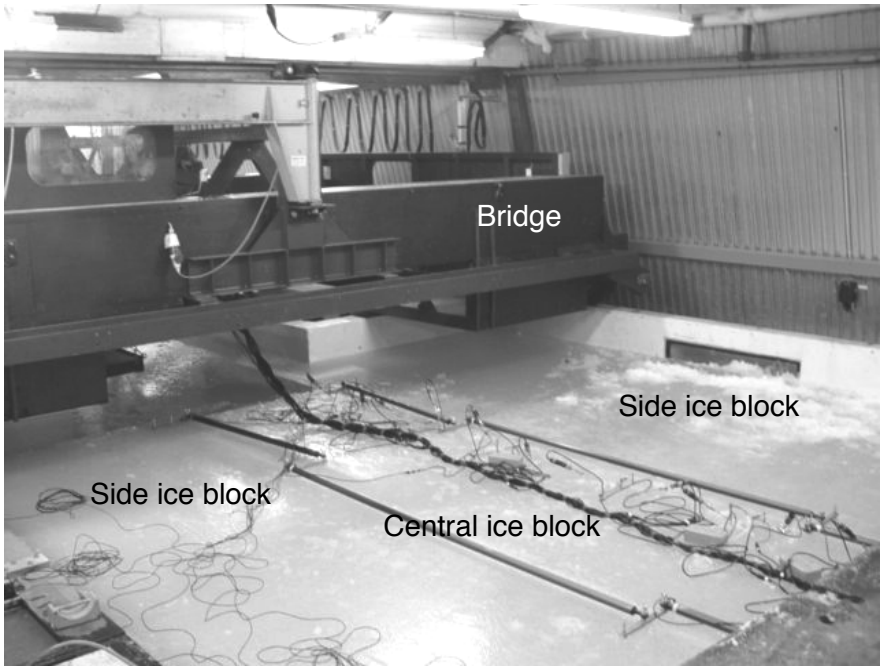

Figure 2

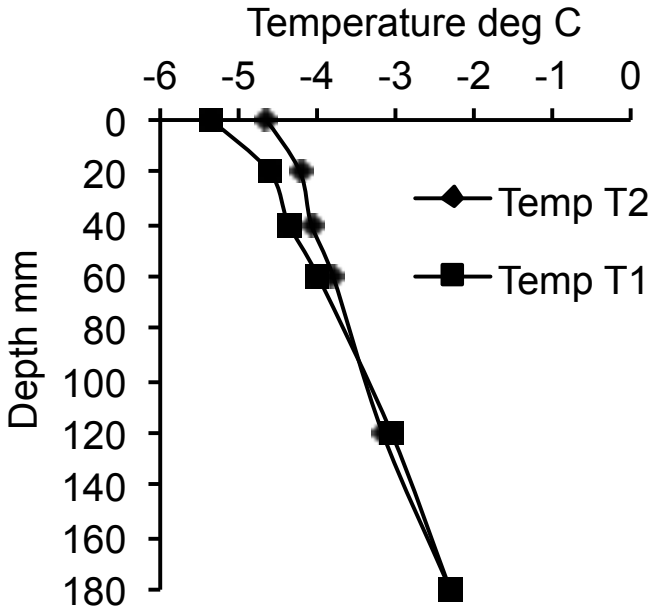

Figure 3

a)

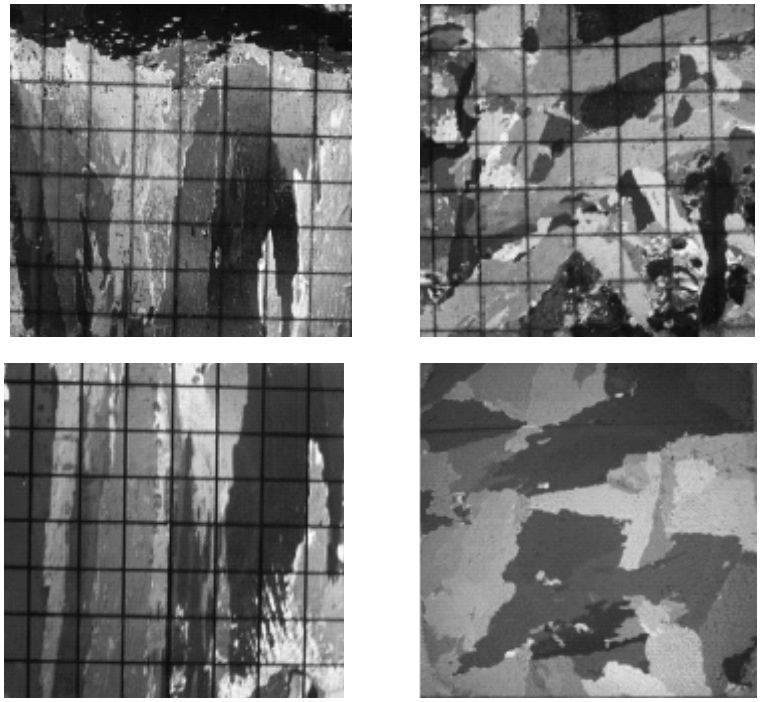

Vertical sections Horizontal sections

b)

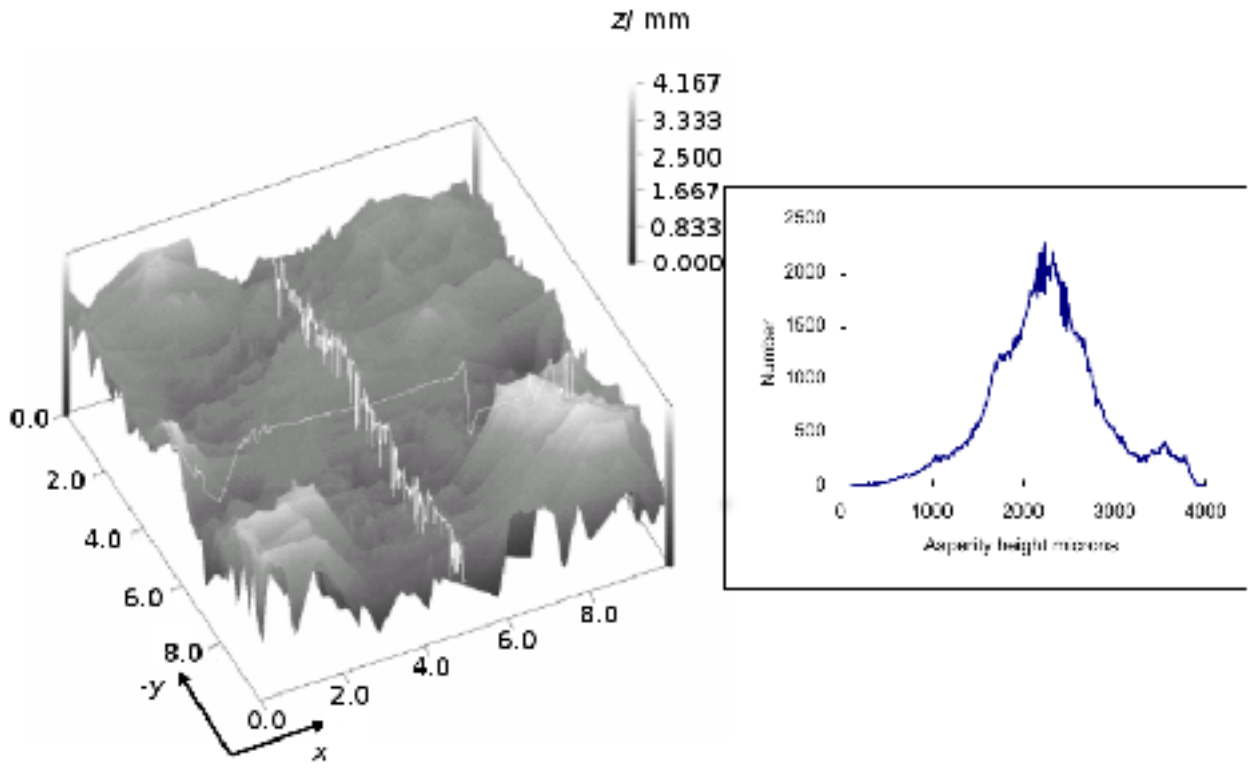

Figure 4

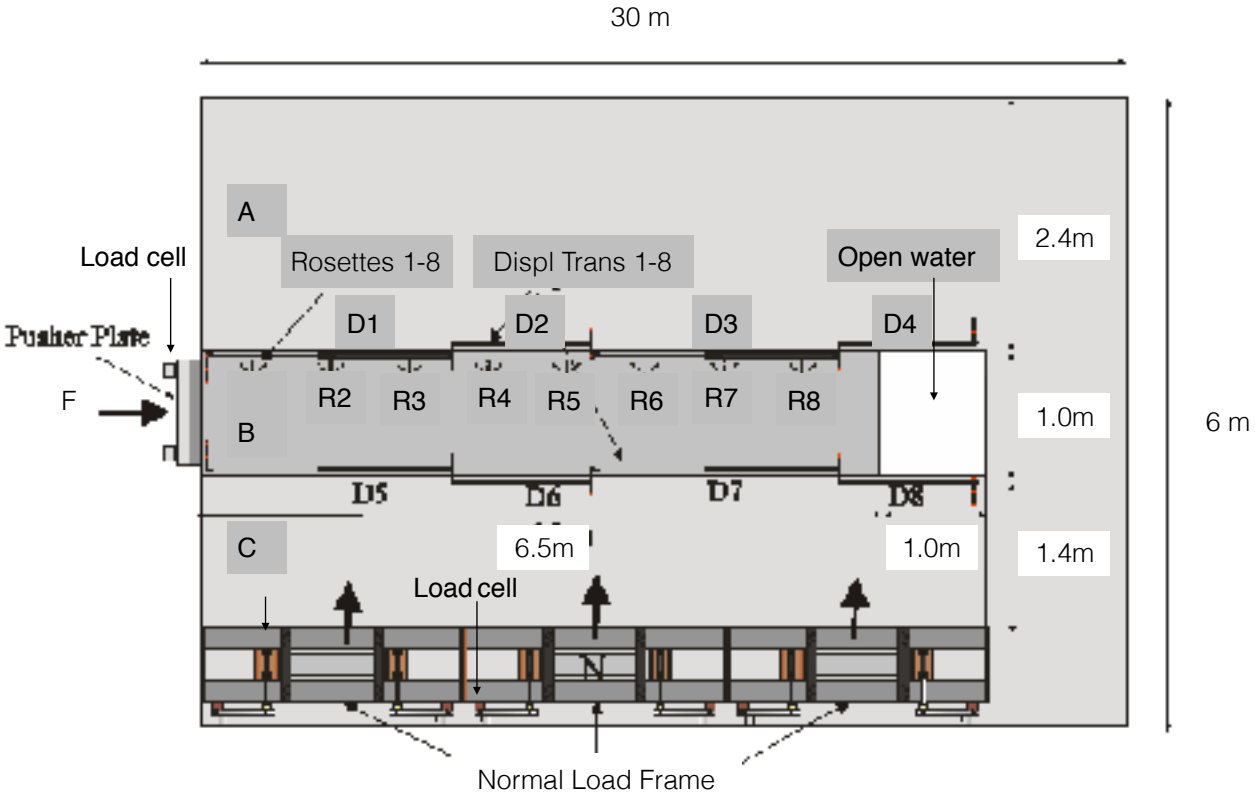

Figure 5

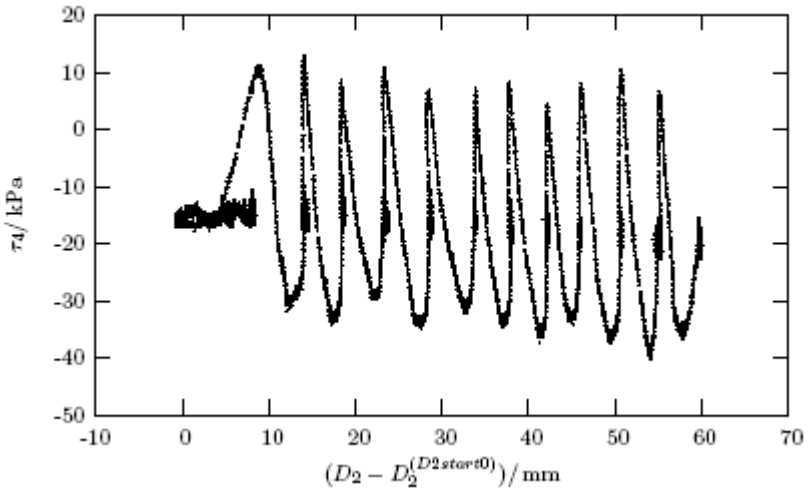

Figure 6

a)

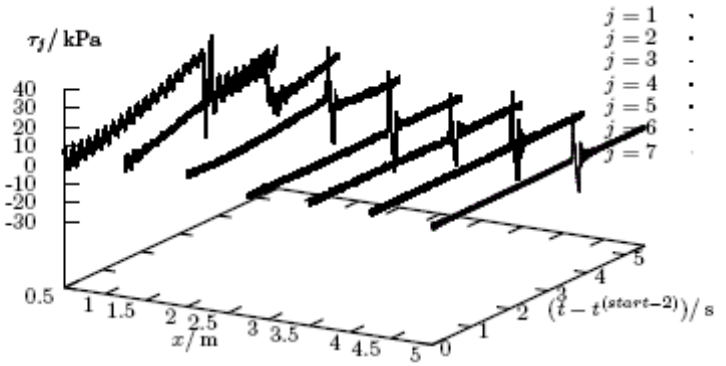
τ_j/ kPa
40
30
20
10
0
-10
-20
-30
0.5
1
1.5
2
2.5
3
3.5
4
4.5
5
x/ m
0
1
2
3
4
5
$(t - t^{(start-2)})$/ s
$j = 1$
$j = 2$
$j = 3$
$j = 4$
$j = 5$
$j = 6$
$j = 7$

b)

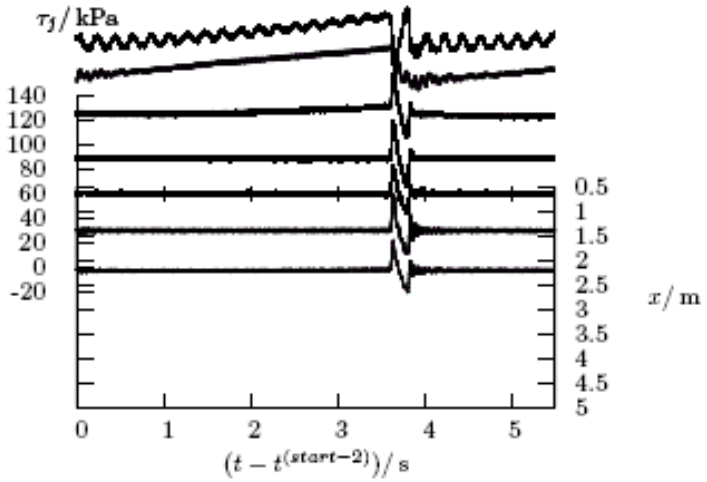
τ_j/ kPa
140
120
100
80
60
40
20
0
-20
0.5
1
1.5
2
2.5
3
3.5
4
4.5
5
x/ m
0
1
2
3
4
5
$(t - t^{(start-2)})$/ s

c)

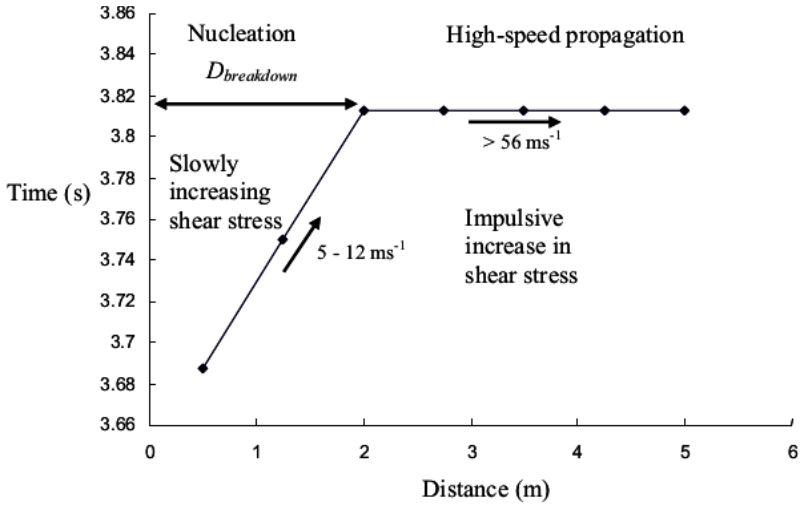
Nucleation
$D_{breakdown}$
High-speed propagation
> 56 ms^{-1}
Slowly
increasing
shear stress
5 - 12 ms^{-1}
Impulsive
increase in
shear stress
Time (s)
3.86
3.84
3.82
3.8
3.78
3.76
3.74
3.72
3.7
3.68
3.66
0
1
2
3
4
5
6
Distance (m)

Figure 7

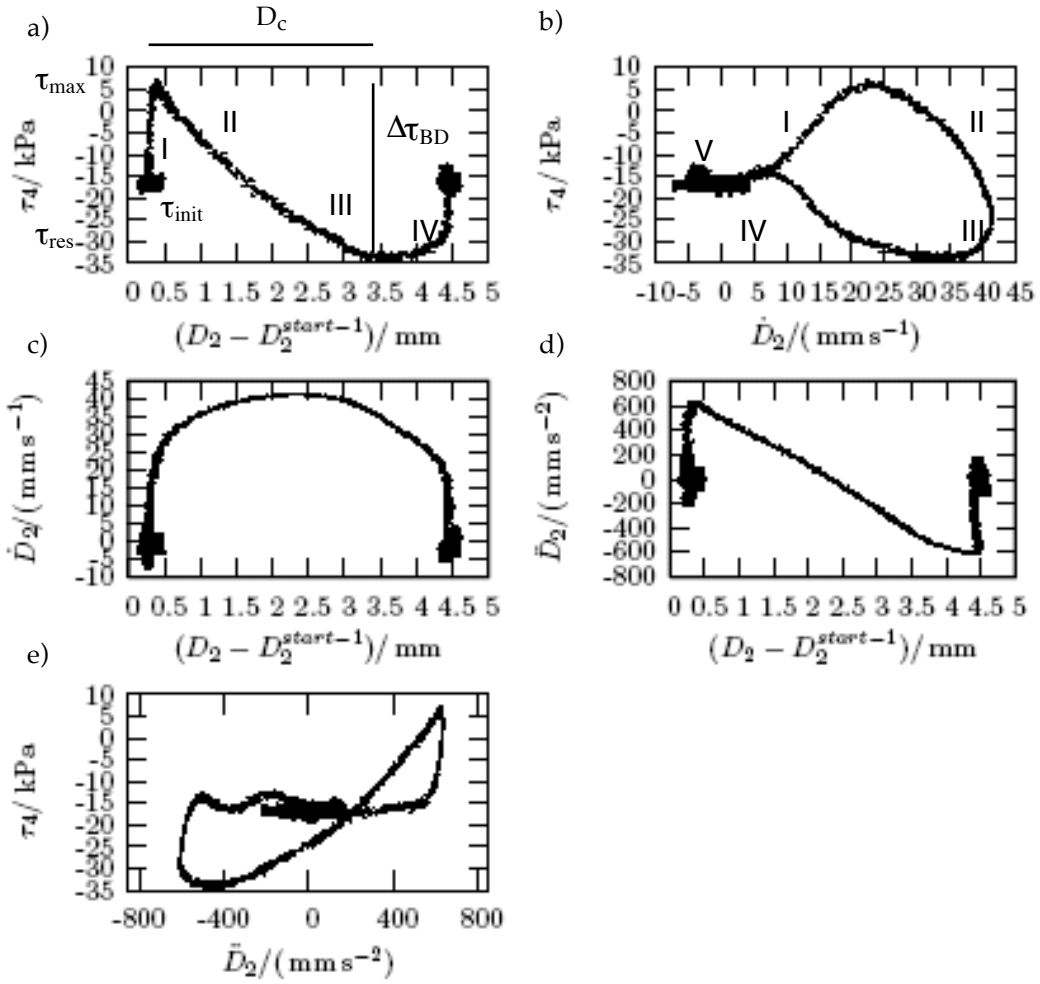
a)
D_c
τ_{max}
τ_{init}
τ_{res}
$\Delta\tau_{BD}$
I
II
III
IV
τ_4/ kPa
$(D_2 - D_2^{start-1})$/ mm
b)
V
$\dot{D}_2/(\mathrm{mm\,s^{-1}})$
c)
d)
$\ddot{D}_2/(\mathrm{mm\,s^{-2}})$
e)

Figure 8

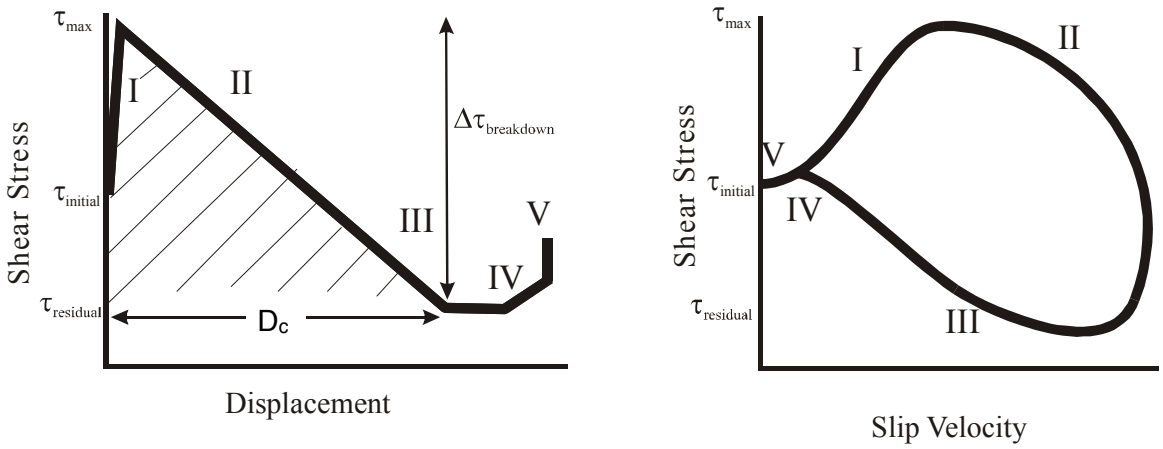
τmax
τinitial
τresidual
Shear Stress
I
II
III
IV
V
Δτbreakdown
Dc
Displacement
τmax
τinitial
τresidual
Shear Stress
I
II
III
IV
V
Slip Velocity

Figure 9

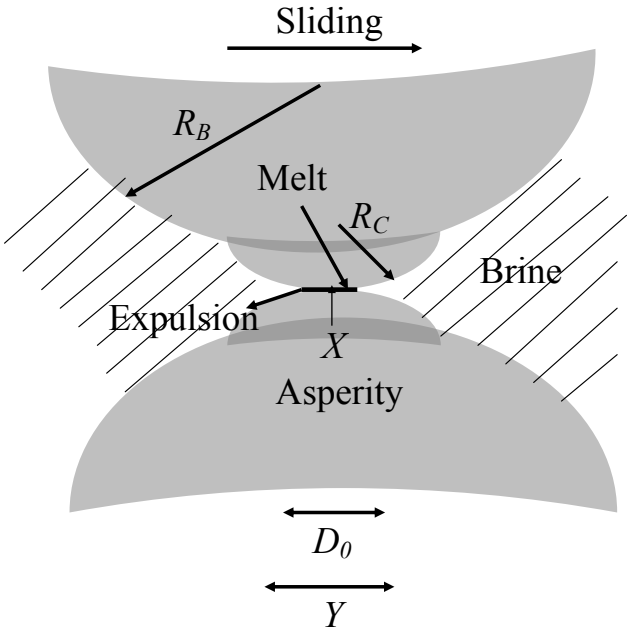

Figure 10

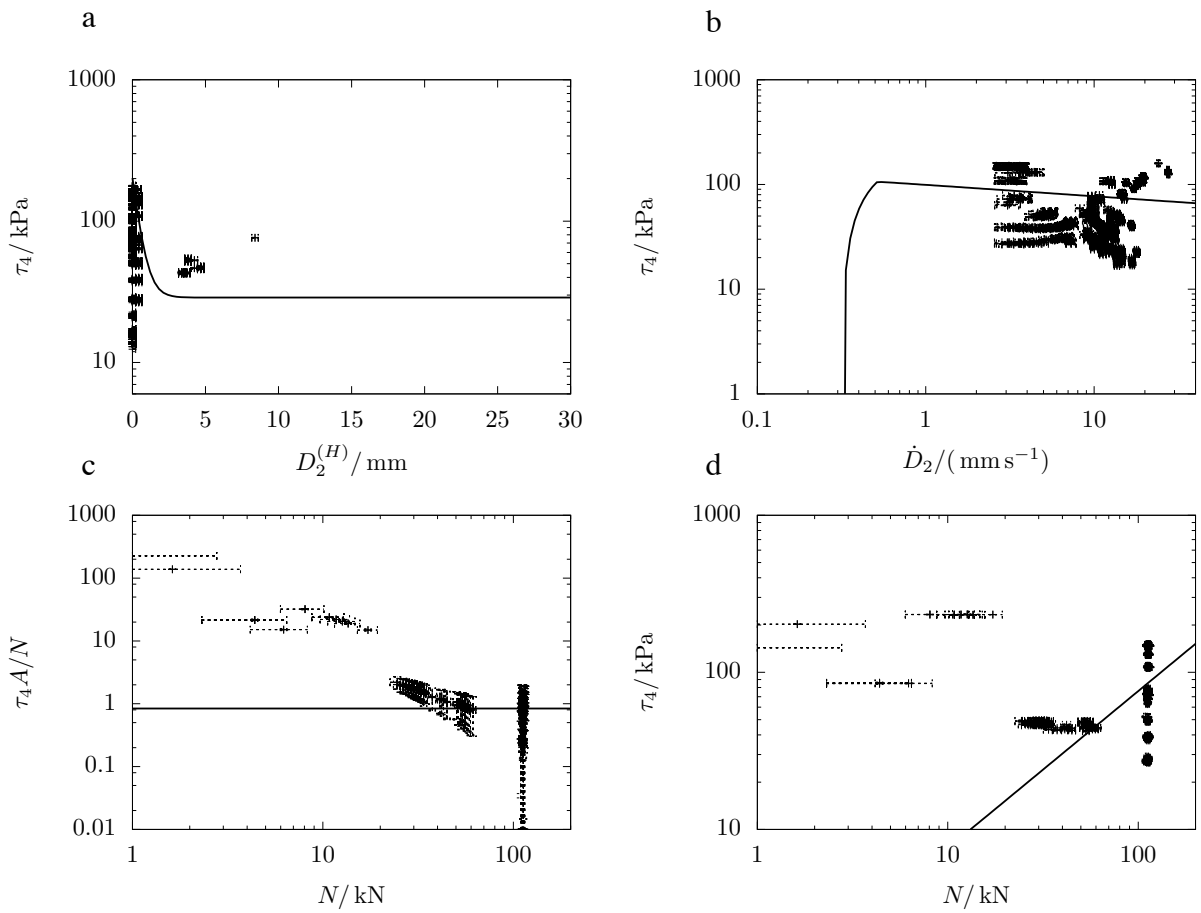

Figure 11

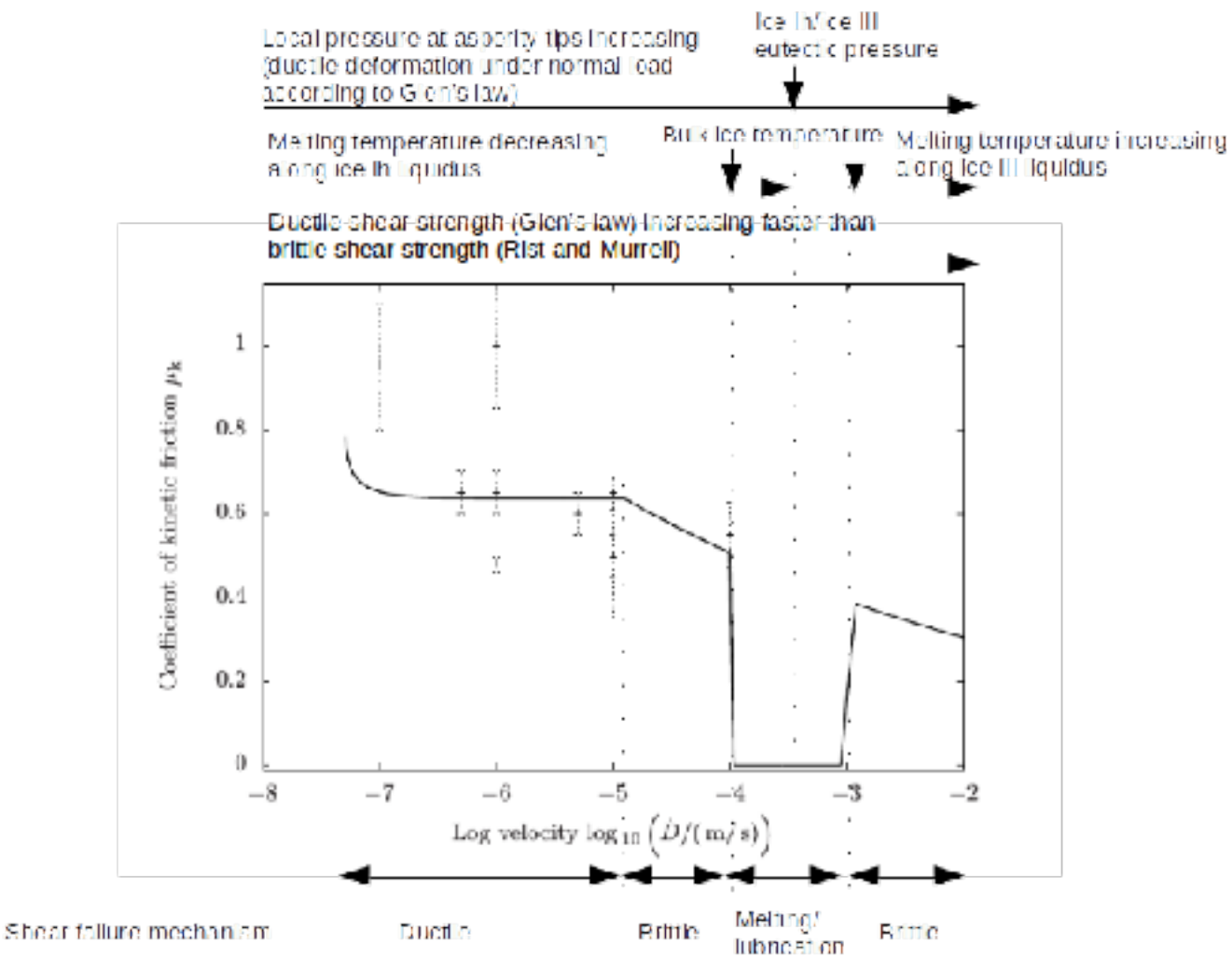
Local pressure at asperity tips increasing
(ductile deformation under normal load
according to Glen's law)
Ice I/Ice III
eutectic pressure
Melting temperature decreasing
along ice Ih liquidus
Bulk ice temperature
Melting temperature increasing
along ice III liquidus
Ductile shear strength (Glen's law) increasing faster than
brittle shear strength (Rist and Murrell)
Coefficient of kinetic friction μ_k
1
0.8
0.6
0.4
0.2
0
−8
−7
−6
−5
−4
−3
−2
Log velocity $\log_{10}\left(D_f/(\mathrm{m/s})\right)$
Shear failure mechanism
Ductile
Brittle
Melting/
lubrication
Brittle